



Coupled DEM-FDM analysis of open-ended pile installation and lateral loading in chalk

Jinhui Zheng¹ · Matteo O. Ciantia^{1,3} · Jonathan A. Knappett²

Received: 24 July 2025 / Accepted: 7 December 2025 / Published online: 22 December 2025
© The Author(s) 2025

Abstract

The in-service capacity of monopiles for offshore wind turbines founded in chalk is a function of the state of the rock around the pile. The installation of a displacement pile affects the fabric of the surrounding rock ('installation effects'). In this paper, a coupled DEM (discrete element method)-FDM (finite differential method) 3D model is used to investigate the installation effects of open-ended displacement piles and their influence on subsequent lateral behaviour in soft rocks. Results indicate that the axial resistance of installed piles in chalk is primarily provided by external shaft and base resistances. In addition, rock material inside the pile cavity experiences a significant dilation behaviour, suggesting traditional indices (incremental filling ratio (IFR) and plug length ratio (PLR)) are unsuitable for evaluating pile installation mode. Considering the distribution of the principal stress, the axial load transfer mechanism for the pile is proposed from a microscale perspective. Subsequent lateral loading simulation reveals that changes in the rock state around the pile due to installation strongly influence lateral stiffness. Finally, macro- and micro-scale analyses confirm that the dominant contributors to lateral resistance are the pile tip region on the passive side and the near-surface region on the active side of the pile.

Keywords Chalk · Coupled DEM-FDM modelling · Installation effects · Rock–pile interaction

List of symbols

C	Cohesion of the bond	g_a	Activation gap of the far-field interaction
d_{00}, d_{50}	Minimum and mean particle size	I_{iner}	Inertial number
D_{pile}	Pile diameter	L_p, L_{pile}	Installed length and pile length
e	Void ratio	p, q	Mean and deviatoric stresses
E_{mod}, \bar{E}_{mod}	Effective moduli of unbonded contacts (inter-particle or particle–pile contacts) and bonded contacts, respectively	R_o, R_i, R^*	External pile radius; internal pile radius; equivalent pile radius
f_L	Axial compression loading factor	t_w	Pile wall thickness
		u_c^n, u_c^s	Softening rate-related parameters along normal and shear directions in the proposed contact model
		v_{pile}	Pile jacking velocity
		ε_a	Axial strain
		θ_c^b	Softening rate-related parameters along rotation direction in the proposed contact model
		$\kappa^*, \bar{\kappa}^*$	Normal-to-shear stiffnesses of unbonded contacts (inter-particle or particle–pile contacts) and bonded contacts, respectively
		$\mu, \mu_{pile-chalk}$	Friction coefficients between the particles and the pile–chalk interface
		σ_c, σ_t	Compressive and tensile strengths of the bond

✉ Matteo O. Ciantia
m.o.ciantia@dundee.ac.uk; matteo.ciantia@unimib.it

Jinhui Zheng
2431370@dundee.ac.uk

Jonathan A. Knappett
jonathan.knappett@eng.ox.ac

¹ School of Science and Engineering, University of Dundee, Nethergate, Dundee DD1 4HN, UK

² Department of Engineering Science, University of Oxford, Parks Road, OX1 3PJ, Oxford, UK

³ Department of Earth and Environmental Sciences, University of Milano-Bicocca, Piazza della Scienza, 4, 20126, Milan, Italy

σ_r, σ_3	Radial stress acting on the pile and confinement
τ_z	Shear stress acting on the pile
ρ	Sample density
Ψ	State parameter

1 Introduction

In recent years, offshore wind energy has emerged as the preferred form of green energy for north-European countries due to their abundant wind resources. In this scope, most existing offshore wind farms are situated in areas with water depths less than 30 m and employ monopile foundations due to their high bearing capacity [1, 63, 74]. During the installation of open-ended piles, the material entering the pile can induce significant friction against the internal walls of the pile, forming a plug that prevents additional material from entering the pile. This is typically referred to as a “plugged” condition. Pile installation can also be unplugged (i.e. coring) and partially plugged. Different plug states have a significant negative effect on pile drivability and load capacity [34, 48].

European wind farms are often located on soft rocks, such as chalk [7, 8, 11]. The primary factors affecting pile drivability and axial bearing capacity in low- to medium-density chalk include end resistance and external and internal shaft resistances. In soil, the relative magnitudes of internal and external shaft resistances are generally closely related to the pile diameter-to-wall thickness ratio and soil conditions (e.g. relative density in sands) [18, 19, 32–34, 41]. In highly porous, soft rocks, however, the installation involves bond breakage and particle crushing, sometime leading to pile free-fall self-weight ‘runs’ as collapsible microstructure, which further complicates the relationship between internal and external shaft friction [29].

To establish a design suitable for monopiles in chalk strata, the joint industry project ALPACA (axial-lateral pile analysis for chalk applying multi-scale field and laboratory testing) conducted systematic research combining advanced field and laboratory tests [2, 7, 8, 38, 62]. The study revealed that the pile driving process remodels the chalk structure, forming fine-grained annuli on both the internal and external sides (chalk putty) [46]. The development of effective stress paths at the pile–annulus interface exhibits similarities to analogous tests in sands, with failure modes following the Coulomb failure criterion and demonstrating constrained interface dilatancy.

Consequently, based on the ICP-05 design method for sand [28], a newly proposed version, ICP-18, was proposed for chalk formations [30]. The ICP-18 method assumes negligible internal shaft friction for offshore monopiles with a large diameter to wall thickness ratio, and this assumption has been validated through signal-matching inversion techniques based on Fibre Bragg Grating (FBG) measurements [9]. This approach effectively addresses the overly conservative estimation of shaft friction (20 kPa) for low- to medium-density chalk in traditional design recommendations [40], providing a more rational basis for the drivability and axial capacity design of open-ended piles in low- to medium-density chalk. However, ICP-18 is primarily based on a limited number of field tests, and the understanding of penetration mechanisms or installation effects caused by pile–chalk interaction remains insufficient. Therefore, further investigation through numerical modelling is warranted.

To accurately evaluate installation effects, continuum-based numerical approaches, such as PFEM (particle finite element method), MPM (material point method), CEL (coupled Eulerian–Lagrangian method) and ALE (Arbitrary Lagrangian–Eulerian), have recently been employed to model pile installation in soils and rocks [21, 45, 54, 59, 60, 64, 69]. The predictive capability of continuum-based modelling is inherently constrained by its constitutive framework. Such models generally cannot resolve key micromechanical processes, including particle rearrangement and force chain evolution, both of which are critical for elucidating the underlying mechanism of open-ended pile installation. The axial load transfer mechanism of OE piles in sand is based on arching [51, 52] and has been shown to be captured using discrete numerical modelling such as DEM [10]. Although pile installation in granular materials has been investigated by many scholars [4, 14, 20, 35–37], only Zhang and Fatahi [70] used DEM to analyse the installation effect of OE piles in cemented soft rocks. However, their simulations, which required a runtime of more than two months, could not simulate large-scale boundary value problems (BVPs) efficiently.

Once in service a monopiles’ lateral response is influenced by the superstructure’s natural frequency, which depends on the foundation’s stiffness [21]. This stiffness is closely tied to the initial state of the rock surrounding the pile shaft. The installation process alters the rock’s microstructure (e.g. by changing porosity and bond degradation), often resulting in a stiffer response and increased lateral capacity. Despite this, most reported studies simulate laterally loaded piles using a wished-in-place (WIP) approach disregarding installation effects [5, 16, 17, 61].

This paper aims to efficiently simulate installation effects of monopile in soft rocks and their influences on

subsequent lateral behaviour. Two model piles with different section sizes and aspect ratios are considered, along with a further case applying WIP installation to investigate the effect of installation method on lateral response. To properly simulate the stress state of the pile and its deformation (e.g. Poisson straining [30]), FDM elements are used to simulate the pile structure, while a coupled DEM-FDM approach is adopted to enhance the computational efficiency [65, 72]. To accurately replicate the softening behaviour of cemented bonds, a recently developed damage bonded contact model is implemented within the DEM zone [73].

2 Novel damage bonded model

The bond damage contact model adopted in this study has been proposed and validated in Zheng and Ciantia [73], where a detailed description can be found. Here, only a brief summary of its key features is provided for completeness. The model is implemented as a user-defined contact model in PFC3D [26].

2.1 Overview of contact law

The model describes the evolution of bonded and unbonded contact forces between particles. The bonded interaction comprises normal and shear forces, as well as a bending moment, while the unbonded interaction is described by a conventional linear contact model. Bond deformation includes both elastic and plastic parts, and the bond damage is characterised by a scalar parameter D_d , which evolves with plastic contact deformation to capture the ductile softening behaviour typical of porous soft rocks such as chalk. By definition, $D_d = 0$ corresponds to an intact bond, whereas $D_d = 1$ indicates complete bond breakage. The full constitutive formulation, yield surface definition, and numerical integration scheme are provided in Zheng and Ciantia [73].

A key feature of this model is the introduction of far-field interactions, which control the activation of unbonded forces. Chemically formed cemented bonds break into several fragments, with some fragments remaining between non-contacting grains hence allowing to transfer some load [13]. This mechanism is incorporated via far-field interactions, as illustrated in Fig. 1a. Furthermore, when bonds are damaged but not yet fully broken ($0 < D_d < 1$), spherical particles in DEM may appear physically separated, while irregular-shaped grains in reality would still have established physical contact (Fig. 1b). Incorporating far-field interactions allows the model to accurately represent this situation. The combination of the damage variable and far-field interactions enables the model to capture the transition from brittle to ductile behaviour in soft rocks under complex stress conditions.

2.2 Model calibration

Model parameters for chalk are calibrated against the results of isotropic and triaxial compression tests from Liu et al. [39], the procedures for which are described in Zheng and Ciantia [73]. The calibrated chalk, a typical porous, soft rock distributed in the North Sea, has a porosity of 0.45 and UCS of approximately 2.8 MPa.

Figure 2 presents the particle size distribution (PSD) of this soft rock and the PSD used in DEM. Currently, only the PSD of destructured chalk (putty) is available. Given that chalk and calcarenite are both porous carbonate soft rocks with comparable structure and mechanical behaviour, the PSD of intact calcarenite is used as a proxy for intact chalk. To meet DEM numerical constraints on particle-size ratios, the intact calcarenite PSD is first equivalently simplified. Comparison shows that intact and destructured calcarenite have similar d_{50} . Based on this, the engineering assumption is adopted that intact and destructured chalk also shares a similar d_{50} . Under this assumption, the “equivalently simplified intact calcarenite PSD” is shifted along the size axis to match the d_{50} of chalk putty, yielding

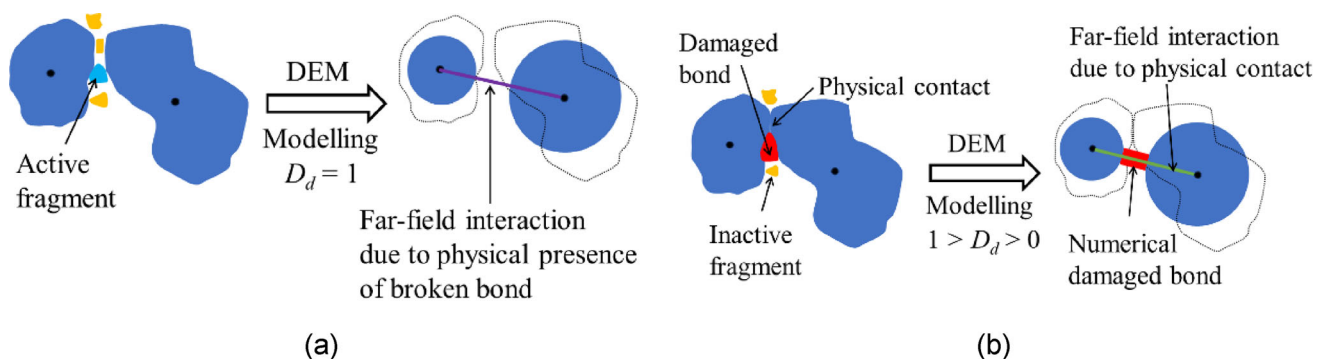


Fig. 1 Schematic diagram of the far-field interaction

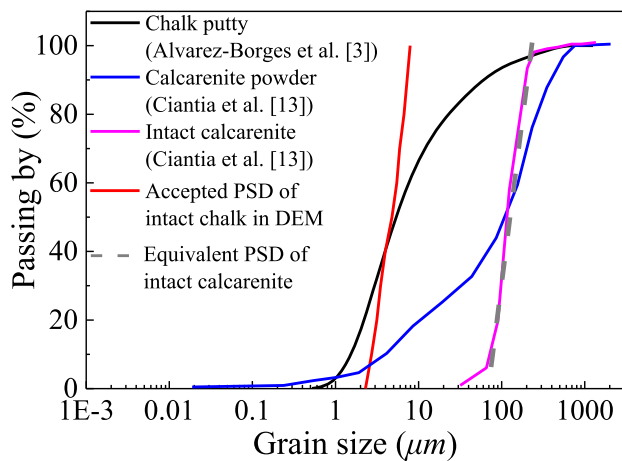


Fig. 2 Particle size distribution of simulated material

a simplified PSD for intact chalk. Please note that the PSDs of destructured chalk and destructured calcarenite are not identical (the latter is broader), so this shift is a reasonable engineering approximation. Numerous DEM studies have shown that, even with simplified or randomly generated PSDs, simulations can reproduce experimental trends at both macro- and micro-scales [37]. Therefore, the proposed treatment is acceptable and practical for engineering analysis.

The simulated chalk sample consists of approximately 24,000 particles and has a height of 76 mm, a diameter of 38 mm and initial porosity of 0.45. The final calibrated parameters and the adopted PSD (particle upscaling ratio = 15) are summarised in Table 1. As shown in

Table 1 Calibrated model parameters and employed PSD for intact chalk

Parameter	Value	Parameter	Value
<i>Unbonded part</i>			
E_{mod}	0.63 GPa	$\kappa^*(\bar{\kappa}^*)$	5
\bar{E}_{mod}	5.5 GPa	μ	0.2
<i>Bonded part</i>			
σ_c	6 MPa	$u_c^n(u_c^i)$	0.03d ₀₀
σ_t	1.5 MPa	θ_c^b	0.01
C	1.5 MPa	g_a	0.13d ₀₀
<i>PSD information</i>			
d ₀₀	0.983 mm	d ₁₀	1.167 mm
d ₂₀	1.350 mm	d ₃₀	1.493 mm
d ₄₀	1.618 mm	d ₅₀	1.747 mm
d ₆₀	1.871 mm	d ₇₀	2.024 mm
d ₈₀	2.222 mm	d ₉₀	2.473 mm
d ₁₀₀	2.708 mm	–	–

$u_c^n=0.23d_{00}$ for compression

Fig. 3a–d, overall a good agreement is observed in both triaxial and isotropic compression tests (note YSL = yield surface line; CSL = critical state line). As the experimental yield envelope is capped, the yield strength of the 104 kPa and 650 kPa confinement pressure tests is quite similar. However, in the experimental results, the post-peak response under low confinement is affected by strain localisation (Fig. 3f), which induces a non-homogeneous deformation within the sample. This explains why the results of test 104 kPa do not agree with the critical state (CS) response observed in the other simulations, which did not exhibit any localised failure patterns. Under low confining pressure, rock failure is dominated by tension-induced cracking, which triggers pronounced stress softening and strain localisation, ultimately forming narrow localised failure bands. In contrast, at high confining pressure, crack opening is suppressed and the failure mechanism shifts towards shear sliding and plastic spreading, leading to more uniform deformation and the absence of localised failure.

3 Coupled FDM-DEM modelling of pile installation

3.1 Model information

The installation process of two small scale piles (tested at 1 – g) is investigated in this section. The model pile experiments that are simulated are reported in Riccio [56], Riccio and Ciantia [57] and Alvarez-Borges et al. [3]. The pile geometries and pile–chalk interface contact parameters are listed in Table 2. The chalk-steel friction angle is about 30° in laboratory tests [53], while a smaller chalk-steel friction coefficient $\mu_{pile-chalk}$ is adopted in Table 2 since model piles are fabricated from polymethyl methacrylate (PMMA, [75]). Additionally, $\kappa^* = 8$ is determined from Wen et al. [66].

Deformation between the discrete and continuous regions is transmitted through a coupling wall attached to the FDM elements at the interface [68]. The coupling strategy operates through the following mechanism: Contact forces between particles and the coupling wall are first converted into equivalent nodal forces applied to FDM element nodes; the deformation response of FDM elements is then computed based on the constitutive model, followed by updating the spatial position of the segments of the coupling wall according to the element deformation; finally, contact forces between particles and the coupling wall are recalculated through the updated geometric relationship at the coupling wall. Further technical details can be found in Zheng et al. [72].

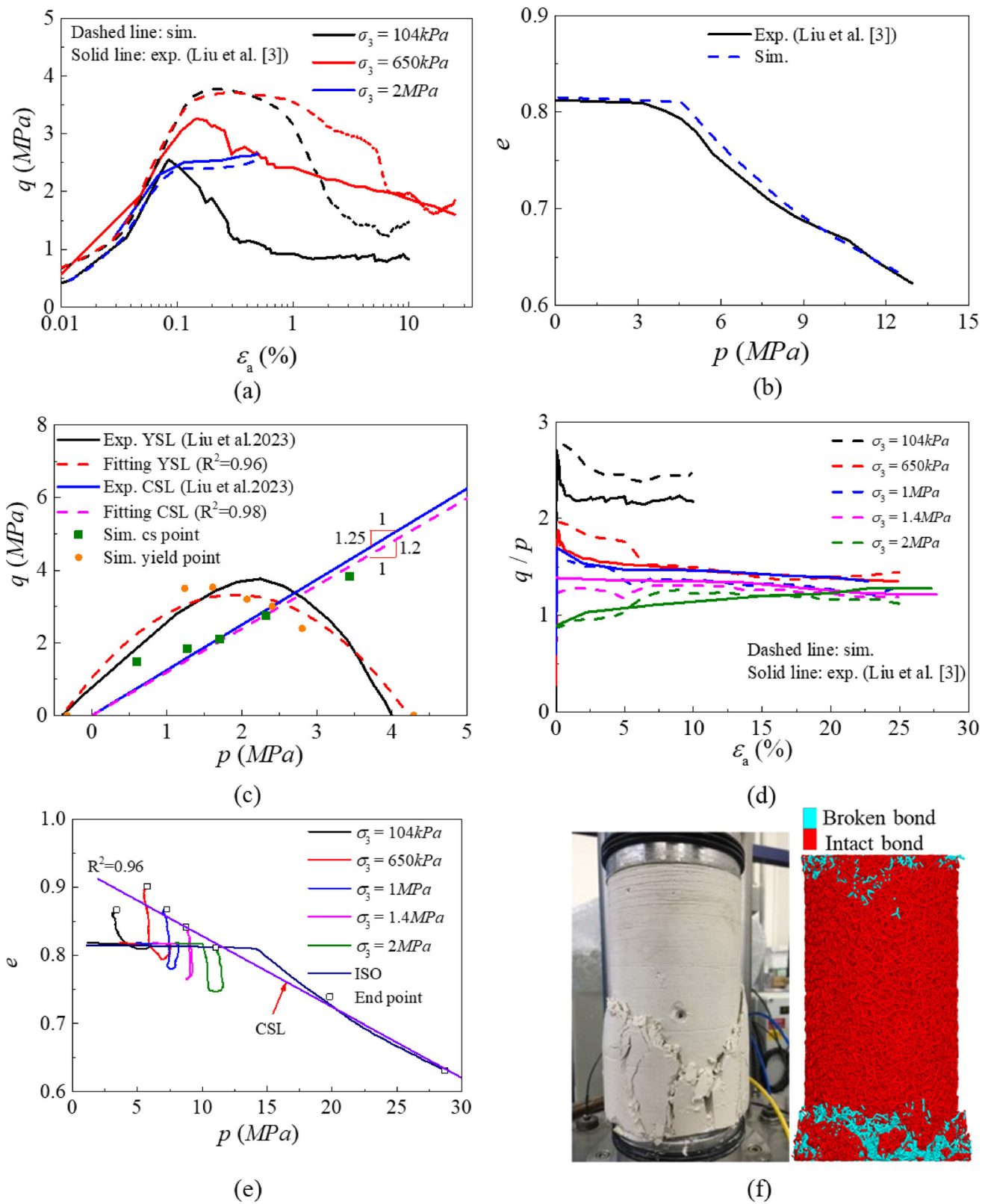


Fig. 3 Calibrated results: **a** triaxial and **b** isotropic tests; **c** YSL and CSL; **d** q/p vs. ϵ_a ; **e** e vs. p ; **f** failure mode (104 kPa) from Pedone et al. [53]

Table 2 Pile geometry and pile–chalk contact information

	Pile A Alvarez-Borges et al. [3]	Pile B Riccio [56]
D_{pile}	8 mm	18.95 mm
t_w	1 mm	0.95 mm
t_w/d_{50}	3	2
L_p	32 mm	36.5 mm
L_{pile}	60 mm	228 mm
E_{mod}	1 GPa	1 GPa
κ^*	8	8
$\mu_{pile-chalk}$	0.3	0.3

As irreversible damage is focussed close to the pile, the constitutive model employed in the FDM region (see Fig. 4) is isotropic elastic, characterised by the elastic parameters of the intact rock (Young’s modulus and Poisson’s ratio of 3 GPa and 0.2, respectively). The geometries of the DEM and combined regions are given in Table 3.

Initial conditions are reproduced using the periodic cell replication method proposed by Ciantia et al. [12] and Zheng et al. [72]. Initial stress conditions consider a lateral earth pressure coefficient K_0 of 0.6 [39, 62]. Particle scaling was used to increase model efficiency without affecting the response of the contact model [73]. Particle refinement is used to obtain an adequate t_w/d_{50} ratio at the interface with the pile, where the upscaling ratios in each zone are indicated in Fig. 5b [44]. Although the t_w/d_{50}

Table 3 Size information of coupled model

	Pile A Alvarez-Borges et al. [3]		Pile B Riccio [56]	
	Diameter (mm)	Height (mm)	Diameter (mm)	Height (mm)
DEM region	40	60	100	60
Whole coupled model	100	135	600	330

ratio in these simulations is smaller than field situations, it is still large enough to avoid particle size effects [10].

3.2 Installation and lateral loading programme

Two piles are jacked to their prescribed depths at jacking velocity v_{pile} determined according to Eq. 1 to ensure quasi-static conditions ($I_{inner} < 0.01$) [27]:

$$v_{pile} = 3D_{pile} \frac{I_{iner}}{d_{50}} \sqrt{\frac{\sigma_3}{\rho}} \tag{1}$$

where σ_3 is the confinement of the sample; I_{iner} is the inertial number of the model (0.01 used in this study), and ρ is the rock density.

For subsequent lateral loading, a constant velocity is only applied on one edge node at the top of Pile B. The loading was quasistatic, and in this case this is achieved by loading at a rate such that the acting contact force and the

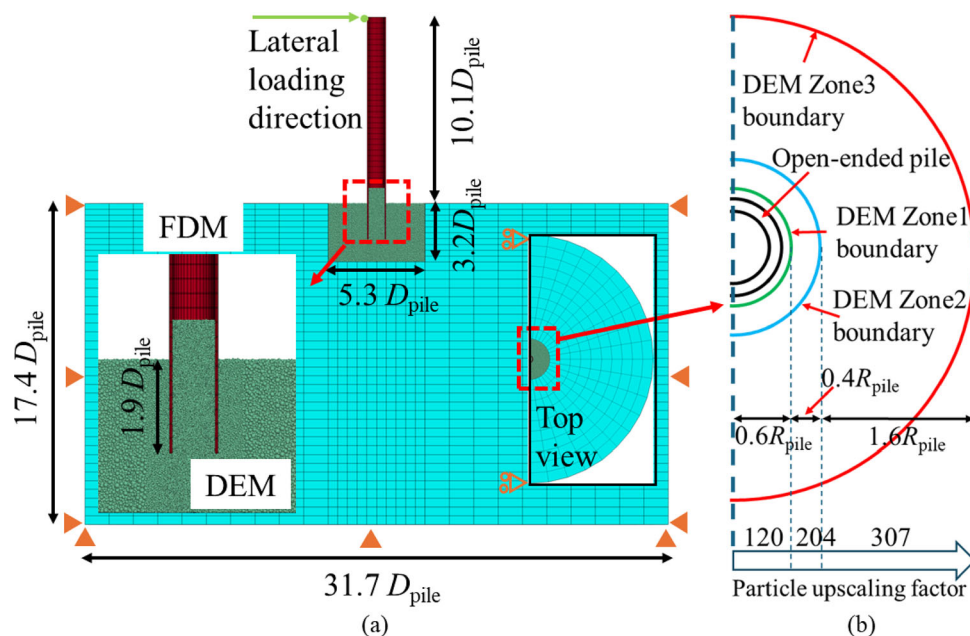


Fig. 4 a model layout and b particle upscaling ratio in DEM region of Pile B

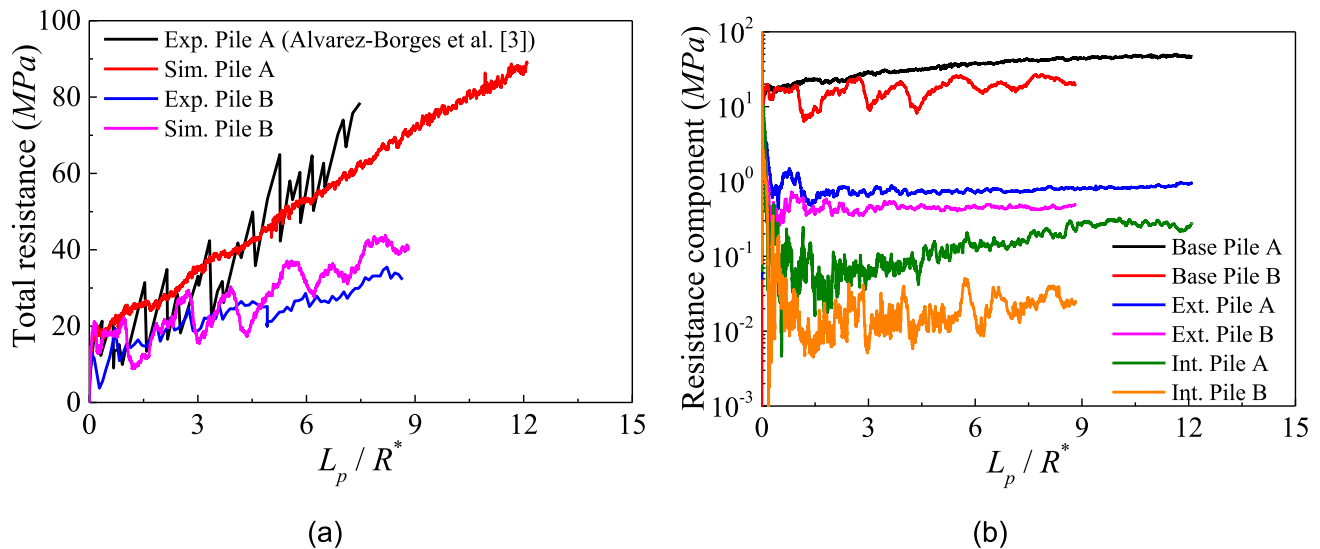


Fig. 5 Comparison of installation resistance vs. installed depth of **a** total resistance and **b** resistance components

unbalanced force of the force applied were equal [31]. The maximum loading rate to achieve this is 0.4 m/s.

4 Installation results

4.1 Macro-response

4.1.1 Penetration resistance

Figure 5 presents the evolution of installation resistance with depth of the two model piles alongside experimental data. Pile A is from Alvarez-Borges [3], while pile B is from Riccio [56]. The installed depth is normalised by each pile's equivalent radius R^* defined as $\sqrt{R_o^2 - R_i^2}$, with total and base resistances normalised by the effective area (πR^{*2}), where R_o and R_i are the external and internal radii of the pile section, respectively. External and internal integrated shaft forces are normalised by their external and internal surface areas, respectively, to obtain shear resistance. A good agreement between simulated results and experimental data is captured in Fig. 5a. In addition, the relatively lower t_w/d_{50} value in Pile B causes the noisier response in Fig. 5b.

Notably, Pile A exhibits higher base resistance and external and internal shaft resistances than Pile B (compared at the same depth normalised by corresponding R^*). This substantial difference can be explained by the ratio of pile diameter to pile wall thickness D/t_w . These ratios are 8 and 20 for Pile A and B, respectively. A smaller D/t_w ratio corresponds to a larger base area, which enhances the confinement effect on the underlying rock beneath the pile wall, thereby increasing the base resistance. Moreover, this

reduced D/t_w ratio promotes the development of higher internal shaft resistance due to the improved lateral constraint.

4.1.2 Stress distributions

Figure 6 presents the distributions of radial and shaft stresses acting on the internal and external portions of the pile shaft at the end of installation. For both model piles, the external stresses (both components) are greater than the internal ones. The internal radial and shaft resistances in Pile A (thicker one, $D/t_w = 8$) are 24% of the external resistances, which is higher than what assumed in field tests in the same chalk [8]. In contrast, the internal radial and shaft resistances of Pile B (thinner one, $D/t_w = 20$) are only 4% of the external resistances. Figure 6 also compares the results with the prediction model by Jardine et al. [30]. The cone tip resistance q_t measured by in situ CPT (cone penetration test) ranges from 10 to 20 MPa [7]. A CPT simulation was also conducted in the same numerical sample, and the simulated q_t is 15.8 MPa. For simplicity, q_t was uniformly taken as 15.8 MPa in the Jardine et al. [30]'s prediction. Furthermore, the value of $f_L=1.33$ is applied in accordance with Jardine et al. [30]. As shown in Fig. 6a, the predicted radial effective stress around Pile A is significantly lower than the simulated values, which is likely attributed to boundary effects caused by the relatively small size of Pile A's coupled model [49]. The predicted shear stresses in Fig. 6c show good agreement with the simulated results, achieved by using the interface friction angle consistent with the model piles considered in the present simulations (16° , see Table 2).

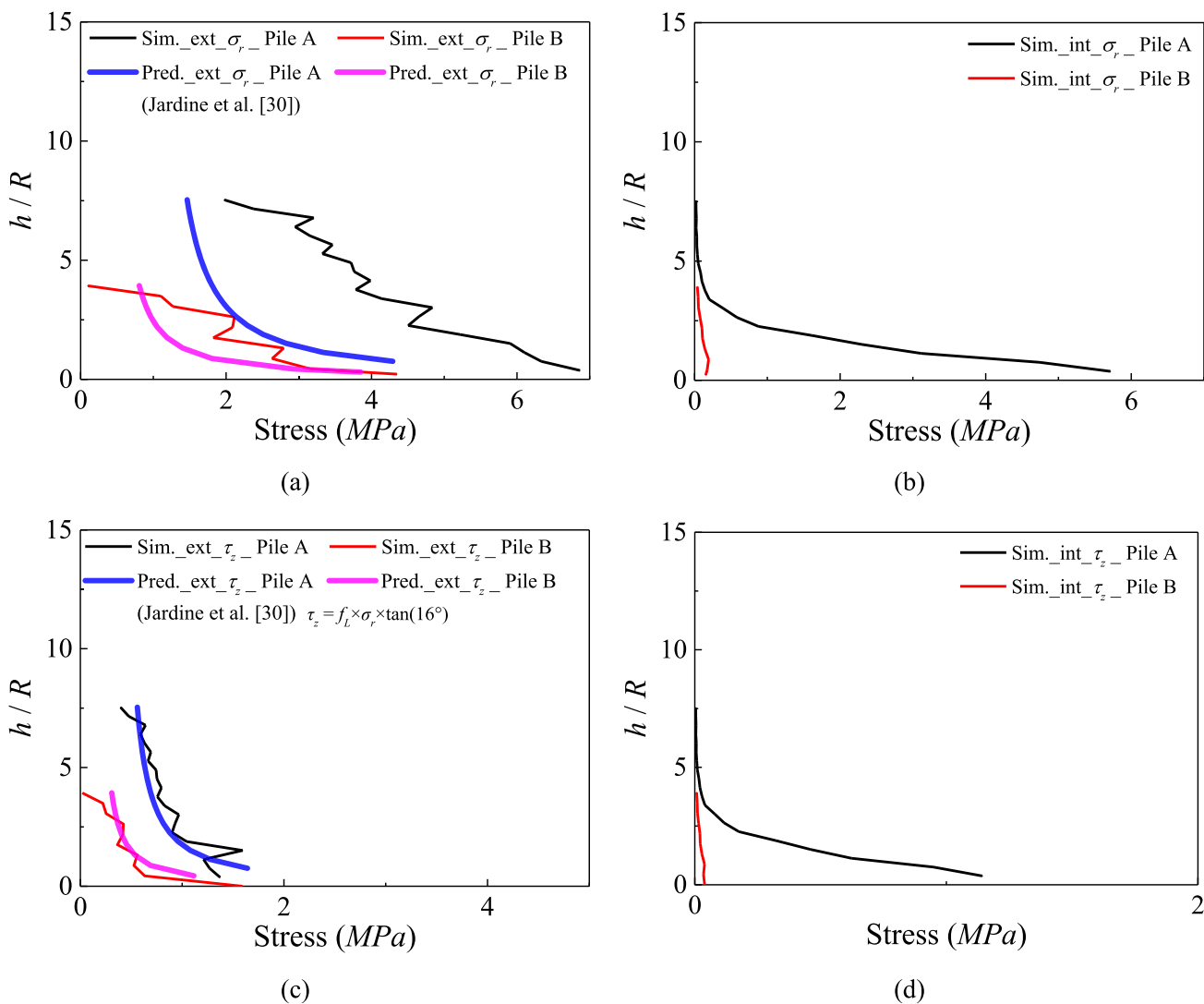


Fig. 6 a and b external and internal radial stresses; c and d external and internal shear stresses distribution along pile shaft

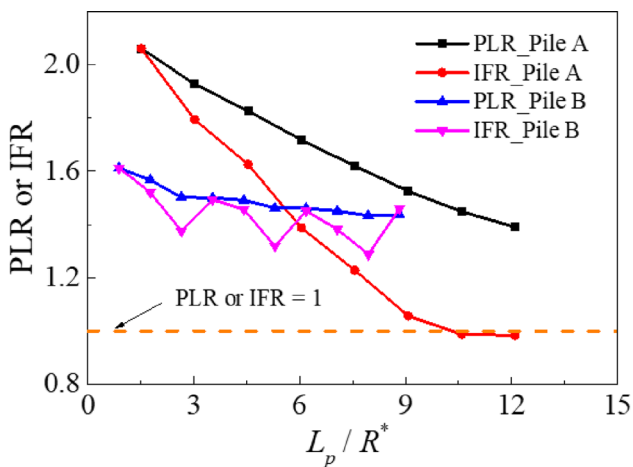


Fig. 7 Evolution of PLR and IFR

4.1.3 Plugging

In Fig. 7, plug length ratio (PLR) and incremental filling ratio (IFR), defined as the ratio of plug length to penetration and its incremental formulation, respectively, are plotted. According to Fig. 7, both Piles A (thicker one, $D / t_w = 8$) and B (thinner one, $D / t_w = 20$) are in an unplugged state (PLR and IFR > 1) [22, 50, 71], although the values are numerically different as these factors vary with the material dilatant behaviour, especially if particle crushing is considered.

For Pile A, the internal shaft resistance increased rapidly during installation, which considerably restrained the growth of the plug height, resulting in a sharp decline in the PLR and IFR with penetration. In contrast, for Pile B, the internal shaft resistance developed gradually. The low internal resistance was insufficient to prevent the influx of

external particles, and thus, the incremental rate of change of the plug height remained relatively unchanged throughout the installation process.

4.2 Micro-mechanical analysis

4.2.1 Porosity

Figure 8 shows the porosity distribution in the DEM region of the two piles. Pile A (thicker one, $D/t_w = 8$) shows a dense region below the pile due to compaction in the ‘nose cone’ region [67]. The presence of a ‘nose cone’ suggests the pile is in a (partially) plugged state. Particles inside Pile B (thinner one, $D/t_w = 20$) have a similar dilatant behaviour to Pile A, though the rock beneath the pile tip remains in a loose state which would suggest an unplugged state for the Pile. The contradictory conclusions between Figs. 7 and 8 demonstrate that the IFR and PLR, which are strongly dependent on material dilatancy behaviour, have limitations in evaluating plugging states in soft rocks. It should be noted that porosity contours of regions close to the pile walls are affected by rigid wall effects [25] combined with particle upscaling, that will both tend to increase the local porosity measures.

4.2.2 Damage zone

Figure 9 shows contours of bond damage state, D_d . For Pile A, the damage zone appears to form a continuous bulb of damaged rock ahead of the pile tip, consistent with the ‘nose cone’ of reduced porosity in Fig. 8a. The width of damage zone external and adjacent to the shaft appears to be related to D/t_w —the pile with a larger D/t_w (Pile B) has a thinner damage zone beneath the pile which is focussed around the pile tip annulus, consistent with an unplugged condition.

Internal bond damage appears to be related to D/t_w and plug state. Pile A with a lower D/t_w has the most severe and uniform internal damage, and this damage zone expands with increasing internal shaft resistance. Traditional theory suggests that the rock below the pile wall undergoes local shear failure [37]. However, due to the small t_w/d_{50} in the current study, the high stress beneath the pile wall is more likely to be caused by pure compression failure. The left half of Fig. 9b shows the damage zone of Pile B when penetrated by 20 mm compared to CT scanning of the pile in the experimental testing [56]. The width of the internal damage zone in the experiment is approximately equal to the pile thickness, while it is larger in the simulation due to the particle upscaling. Experimentally observed internal cracks in the right half of Fig. 9b are captured in simulations, indicating the

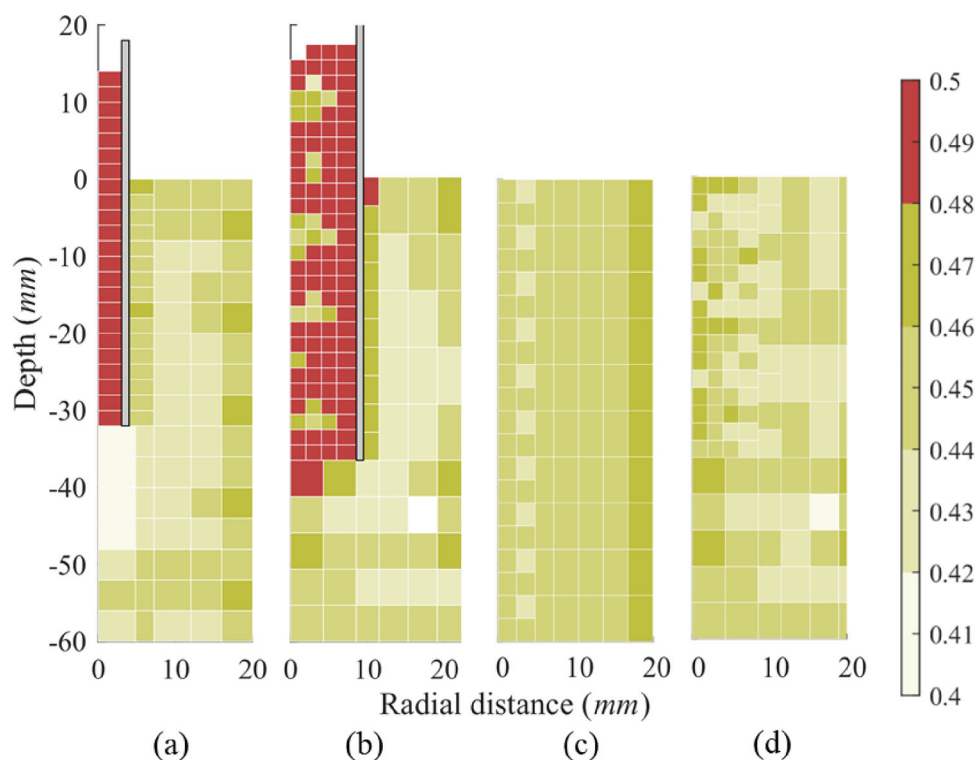


Fig. 8 Porosity distribution in the DEM region: **a** Pile A and **b** Pile B after installation; **c** Pile A and **d** Pile B before installation

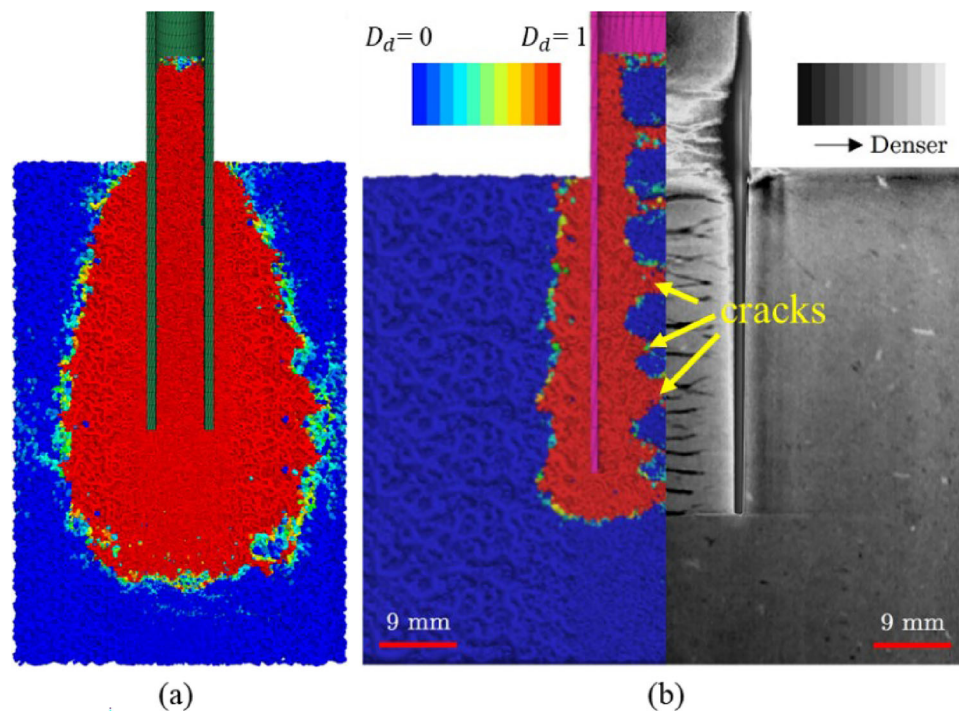


Fig. 9 Damage zone distribution in the DEM region: **a** Pile A ($D/t_w = 8$), **b** Pile B ($D/t_w = 20$). The μ CT image is taken from [56]

performance of this model to replicate the initialisation and propagation of cracks. These cracks are macroscopic responses to microscopic bond breakages.

The horizontal cracks that develop inside the plug may also contribute to the noisier response for Pile B that is shown in Fig. 5b, in addition to the effect of relatively lower t_w/d_{50} that was previously noted. Furthermore, particle scaling affects the thickness of these openings which are larger than those observed experimentally. This, in turn, may induce larger transient drops in penetration resistance.

4.2.3 Particle displacements

In Fig. 10, the position of different rock sublayers inside the pile can be explained according to the deflection effect for open-ended piles proposed by Paikowsky and Whitman [51] and Paikowsky et al. [52]. The convex upward deflections (rock moved upwards compared to its initial position) at the upper zone inside the pile are caused by the low internal shaft friction on the rising material. Downward deflections occur in the Pile A, indicating the relatively larger internal shaft resistance if formed inside the pile. The downward deflections (rock moved downwards compared to its initial position) form a nose cone region beneath the pile tip, corresponding to the densification zone below the annulus in Fig. 8a. Rock particles in this zone remain approximately stationary relative to the pile shaft. It also demonstrates that the presence of downward deflections is indicative of a plugged state. The distribution of

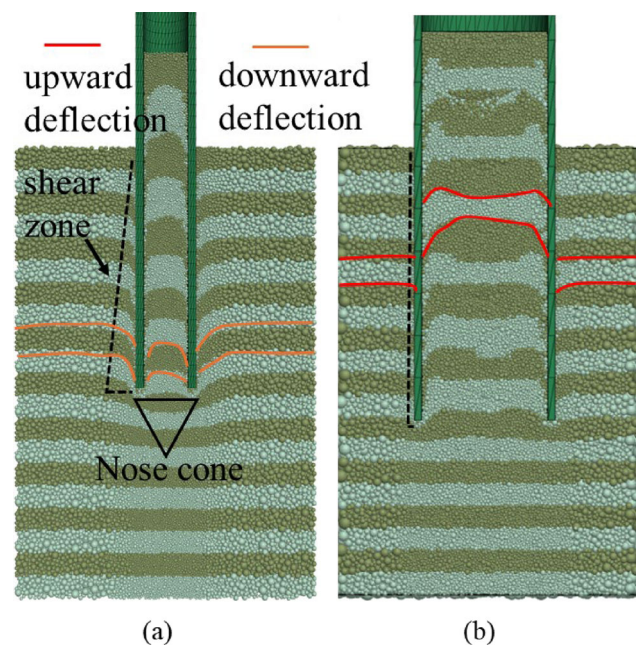


Fig. 10 Deflection distribution in the DEM region: **a** Pile A and **b** Pile B

deflections supports PLR and IFR being insufficient to describe the plugging state. In addition, rock particles adjacent to the external pile wall are dragged downward by shaft friction, with the shear zone width in Fig. 10 progressively decreasing upward from the pile end as indicated by the black dash line. This distribution pattern

correlates with the external shaft resistance profile shown in Fig. 6b. Compared to Pile A, only downward deflections were observed within Pile B, with no discernible nose cone formation detected beneath its tip.

4.2.4 Axial load transfer mechanism

The force chain direction for load transfer closely follows the trajectory of the principal stress [52]. The magnitude and distribution of the principal stress around Pile A (thicker one, $D/t_w = 8$) and Pile B (thinner one, $D/t_w = 20$) after installation are illustrated in Fig. 11a, b. Based on the distinct distribution pattern of the principal stress, the distribution of principal stress within the range of one pile diameter can be categorised into 4 zones, as depicted in Fig. 11c (similar to Li et al. [36]). In the top zone (surcharge zone), the material experiences significant dilation (see Fig. 8a, b), resulting in smaller principal stress magnitudes and inhomogeneous rotation. This zone can be regarded as the overburden [55]. In the bottom plug zone, the vertical principal stresses near the pile wall are deflected towards the pile wall, with greater deflection closer to the pile wall, indicating the gradual development of inner friction from the pile wall inward. All three principal stresses in the nose cone are significantly deflected, indicating that the rock in this region mainly experiences a mixed type of deformation. Material in the nose cone region is subjected to radial force from the arch beneath the wall, the downward force from the plug and the lower upward reaction force combined, such that the rock in this zone undergoes combined vertical and lateral compression deformation. Finally, the rock in the densification zone is constrained by vertical compression.

Figure 11a, b presents idealised schematics of arch formation beneath the pile wall for the two piles. The arch geometry corresponds to the distribution of strong force chains beneath the wall and can be defined by the position of the outermost continuous strong force chain. Post-installation force-chain maps show that a coherent chain forms beneath Pile A, giving an arch rise of approximately $0.75D_{\text{pile}}$, whereas Pile B exhibits only localised strong chains within about $0.3D_{\text{pile}}$ from the wall (Fig. 11d). Arch stability is determined by the continuity of strong force chains: an unbroken compressive path connecting the two arch bases indicates a more stable arch; interruption by cracks/voids implies an unstable arch.

Figure 11 further reinforces the concept that both external and internal friction gradually develop from the bottom to the top and from the pile wall towards the centre of the pile. The formed complete arch below the pile prevents external particles from entering the internal pile cavity, leading to a constant plug height.

4.2.5 State of destructured rock during installation

To explore the origin of installation resistance in sands, Martinelli and Pisanò [42] and Spyridis and Lopez-Querol [58] analysed the evolution of stress paths in sand during pile penetration with reference to the CSL and evaluated the prediction of the state parameter for volumetric response. A similar analysis for Pile B is given in Fig. 12. The arrangement of monitoring points (MP) is as follows: MPs 1–3 along the pile shaft are positioned at a horizontal distance of one pile wall thickness from the pile surface, while MP4 is located vertically beneath the pile tip at a distance of one pile wall thickness. The radii of these MPs are $3d_{50}$. To accurately characterise the evolution of rock state, a three-stage marking method is adopted in the figure to clearly illustrate the stress–void ratio paths at each monitoring point: squares represent the initial state, upward triangles indicate the state when the pile tip reaches the depth of the monitoring point, and downward triangles correspond to the unloading stage after the pile tip passes the monitoring point.

Monitoring data show that significant dilative behaviour is observed at all monitoring points except for MP4 directly beneath the pile tip (Fig. 12d). Specifically, during the initial stage of penetration (before the pile tip reaches the depth of the monitoring points), the void ratio at each point remains relatively constant with increasing mean stress. Once the pile tip reaches the depth of a monitoring point, the void ratio exhibits a sharp increase. Among them, MP2 shows the greatest rate of increase due to crack formation within the pile induced by penetration. In the unloading stage, except for MP2 where crack presence leads to a disrupted stress path, the dilative behaviour at other points tends to stabilise. It is noteworthy that MP4 undergoes continuous densification under the high pressure from the pile tip.

The study identifies three key phenomena: first, the stress states at MPs 1–3 remain significantly higher than their initial values even after unloading; second, the pronounced dilation at MPs 1–3 is likely to trigger internal structural collapse within the soft rock, which may help explain the “free fall” sometimes reported in the field. The state parameter is defined as $\Psi = e - e_{cs}$, where e_{cs} and e are the critical-state and current void ratios under the same stress, respectively. $\Psi > 0$ in the initial state indicates a looser state with a contraction tendency upon shearing, whereas $\Psi < 0$ initially indicates a denser state with a dilation tendency. All cases show a positive change in Ψ as installation proceeds, indicating dilation. It should be emphasised that, although Ψ is commonly used to describe the volumetric tendency of sands [6], it does not explain the abnormal dilation tendency observed at MPs 1–2 ($\Psi >$

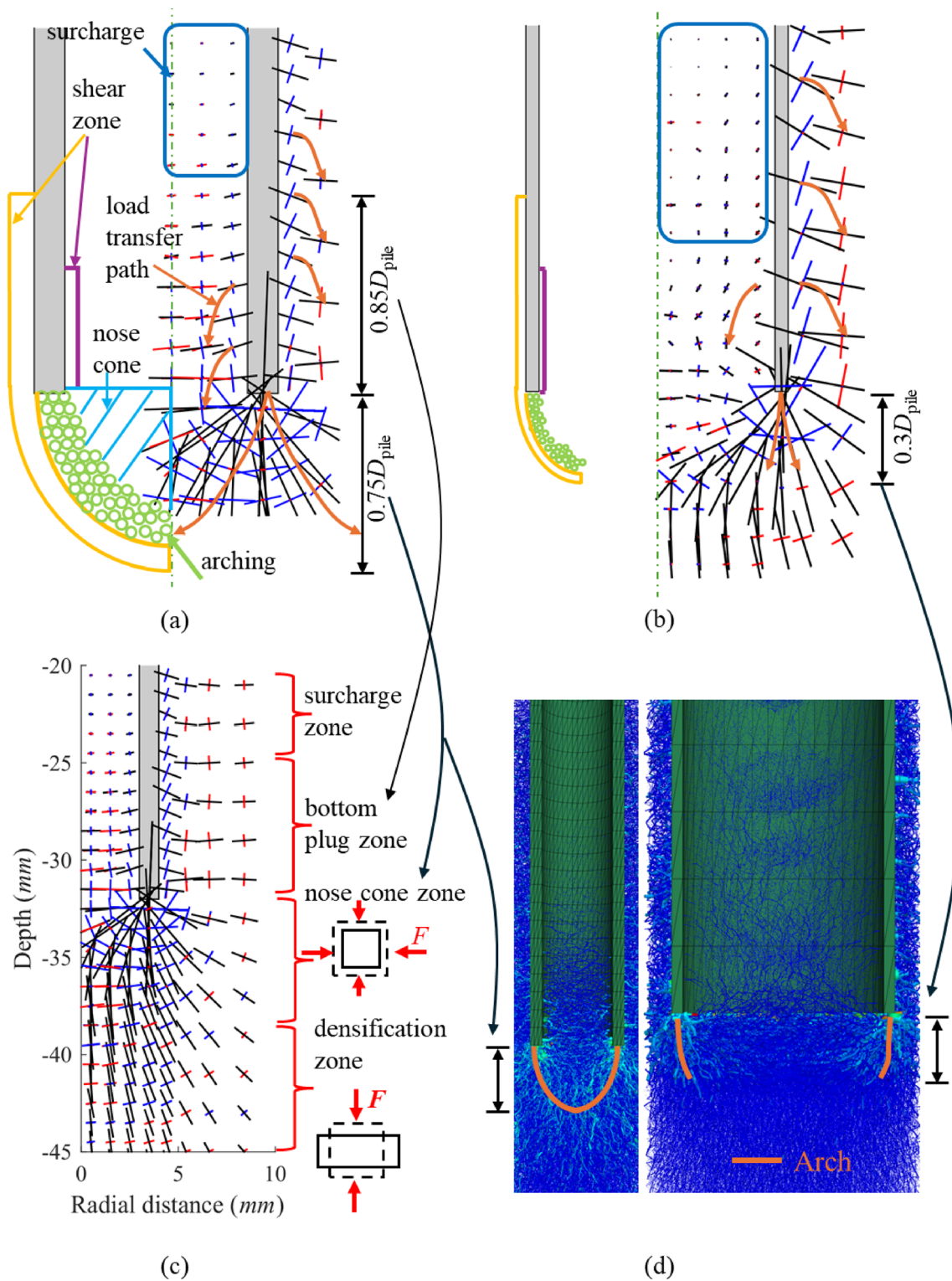


Fig. 11 Sketch of axial load transfer mechanism: **a** Pile A; **b** Pile B; **c** category of principal stress (line length represents stress magnitude but two piles are plotted with different scales, red, blue and black colours mean the principal stress in x-, y- and z-directions); **d** force chain and arch distributions (left: Pile A; right: Pile B)

0) in destructured chalk. This abnormality is attributed to crack formation during the penetration of Pile B.

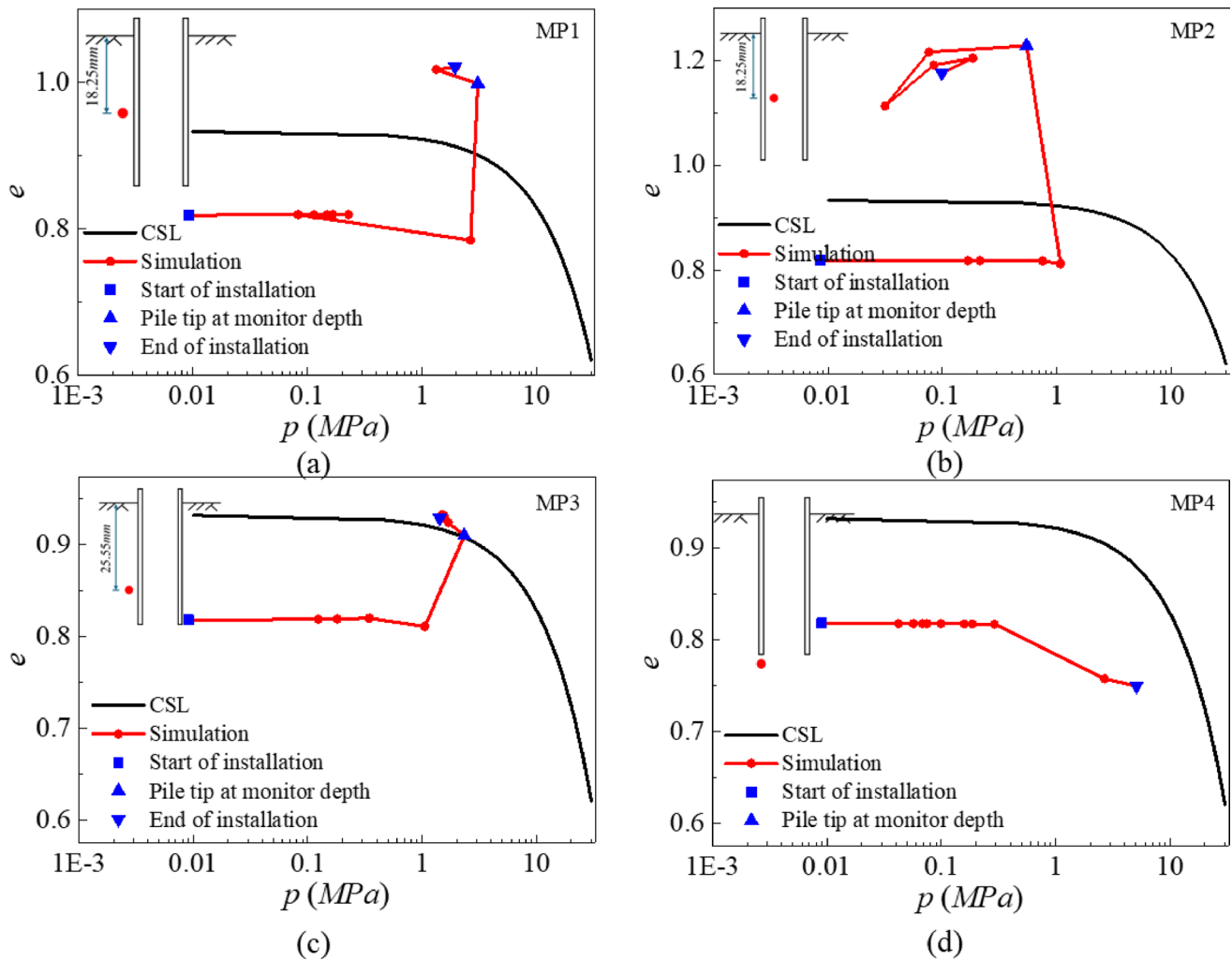


Fig. 12 Mean stress–voids ratio space during installation: **a** MP1; **b** MP2; **c** MP3 and **d** MP4

5 Lateral loading results

5.1 Global lateral response

Pile lateral response following previous installation effects is investigated here by comparing the jacked Pile B (with higher D/t_w closer to real OWT monopiles) and wished-in place (WIP) simulations. In Fig. 13, the WIP case has a 50% greater initial stiffness due to the intact microstructure of the surrounding rock compared to the jacked case. Installation effects appear to induce a minimal change in the ultimate lateral capacity ($< 2\%$ when the pile top displacement is $0.1D_{pile}$), as also reported in the pile simulations in sand conducted by Staubach et al. [59]. The simulation results appear to accurately predict the experimental data in terms of the initial stiffness, yield load and ultimate load. Consistent with the microstructural observations (Fig. 9), the stiffness reduction in installed Pile A

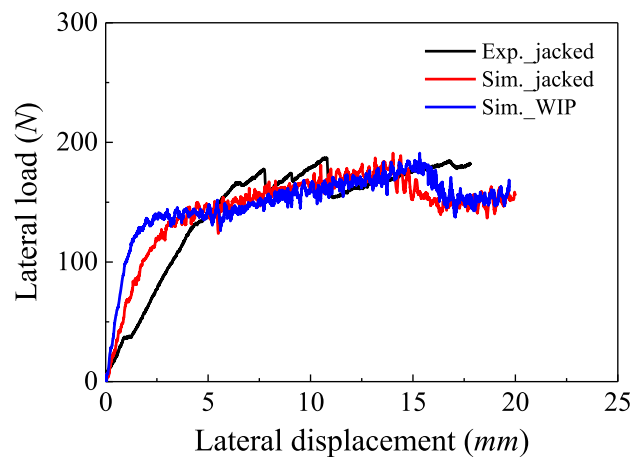


Fig. 13 Load vs. pile top displacement

(relative to its WIP counterpart) should exceed that of Pile B, owing to more extensive plug-induced damage.

5.2 Micromechanical results

5.2.1 Rock flow mode

As presented in Fig. 14, the pile undergoes rigid-body rotation with a centre of rotation located at a depth of $0.5L_p$ below the ground surface. A gap is observed on the active side between the rock near the ground surface and the pile shaft, which is expected to significantly influence the shape of the load deformation (p - y) response during cyclic loading [15, 43]. On the passive side, the rock near the ground surface exhibits heave, allowing the slip surface to be clearly inferred. The area enclosed by this surface corresponds to the wedge-shaped failure zone of the soft rock. Figure 14b–d presents particle movement patterns across cross sections at different depths, where arrows indicate displacement directions, and arrow colours represent displacement magnitudes. The flow modes on the three planes are similar, and no flow-around behaviour—commonly observed for laterally loaded piles in soils [23]—is identified at any depth. According to Murff and Hamilton [47], this suggests that the ultimate lateral capacity should be similar at varied depths, a conclusion which is confirmed by the field tests conducted by McAdam et al. [43].

Figure 14a additionally demonstrates that the lateral displacement is primarily concentrated near the pile. According to Pedone et al. [53], when the lateral displacement at the mudline reaches $0.1D_{\text{pile}}$, the plastic deformation zone extends up to a maximum of approximately $25t_w$ beyond the pile wall. In the present simulation, the lateral displacement at the mudline is approximately

$0.02 D_{\text{pile}}$, and the FDM region is located $33t_w$ away from the pile wall. Furthermore, the deviatoric stress in elements near the DEM-FDM interface at the mudline is approximately 1.2 MPa, which is lower than the triaxial yield stress under corresponding low confining pressures. These observations support the appropriateness of the elastic model used in the FDM region.

5.2.2 Stress and bond damage fields

Comparing Fig. 15a, b, a significant radial stress increase is observed in the rock below the zero-deflection point on the passive side and above it on the active side in the jacked pile. These regions are the main areas that provide lateral resistance and demonstrate that the plug has no significant effect on lateral capacity of the jacked pile. In addition, intense shearing occurs below the pile tip due to toe-kick. Figure 15 also suggests that a pile which would be typically considered unplugged still can produce a significant alteration to the stress field during installation, which is opposite to the point proposed by Hu et al. [24]. During lateral loading, the area where stress increases significantly corresponds to the area where bond damage propagates (Fig. 16). For the WIP pile case, the distribution of external high-stress zones closely matches that of the jacked pile (Fig. 15d), with identical patterns observed in the external damage regions (Fig. 16d). However, significant stress field modification is observed within the plug, particularly near the pile tip. Comparative analysis of Fig. 15b–d conclusively demonstrates that the plug has a substantial

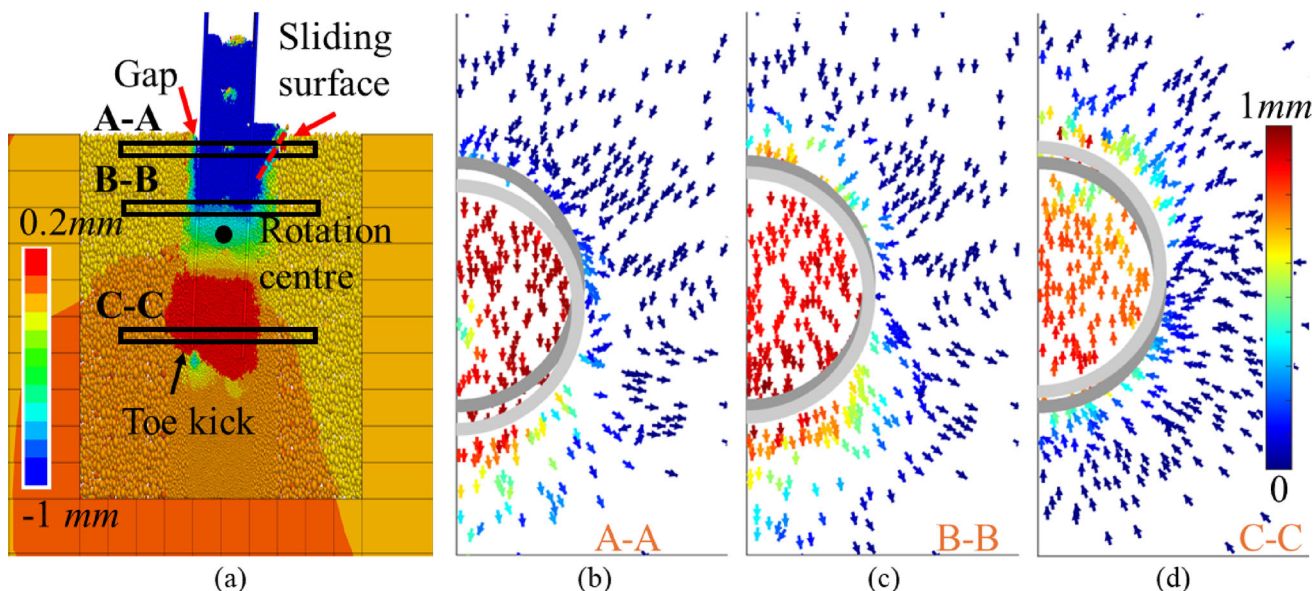


Fig. 14 **a** side view of displacement field; **b** to **d** rock flows on different planes (dark and light grey semicircles are the original and current positions of the pile, respectively)

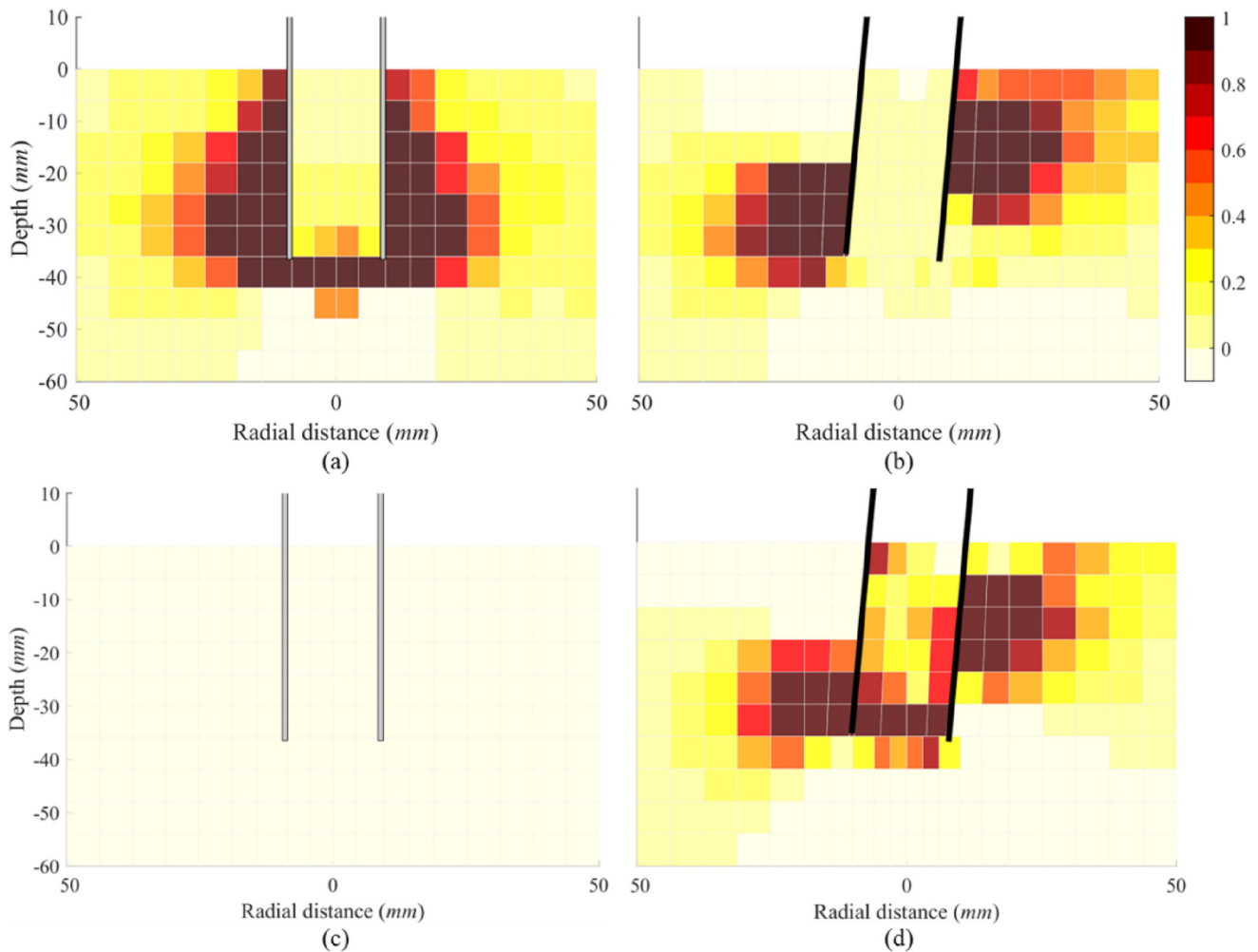


Fig. 15 Radial stress field of the Pile B: **a** after installation; **b** after lateral loading of the jacked case; **c** after installation; **d** after lateral loading of the WIP case (unit: MPa)

effect on the lateral response of the WIP pile during initial loading stages (prior to rock damage beneath the plug).

5.2.3 Particle connectivity

Particle connectivity is defined as the average coordination number of all particles within each probe bin. Here, the change of particle connectivity during lateral loading is used to interpret stress changes around the pile for a jacked pile and for a WIP pile. Figure 17 shows the distribution of the change in connectivity between the end of pile installation and the end of lateral loading. The change in connectivity for each bin is calculated by subtracting the pre-lateral loading connectivity from the post-lateral connectivity, where negative values indicate contact reduction. The regions with reduced connectivity in Fig. 17b correspond closely to the areas of stress increase shown in Fig. 15d, whereas the regions experiencing stress relief in Fig. 15b align with those showing reduced connectivity in

Fig. 17a. A significant drop in connectivity within the wedge-shaped failure zone and persistently stable connectivity near the pile tip are clearly observed in Fig. 17a. In these regions, the breakage of inter-particle bonds during the installation process creates a crushed rock annulus that inhibits the increase in connectivity even in the passive regions around the pile. This is likely because the putty has reached a critical state (see Fig. 12) where it is known that even connectivity reaches its “steady” state [14]. Therefore, unlike that in the WIP pile, particle connectivity in passive zones shows no increase adjacent to the jacked-pile walls during lateral loading.

To further explore the link between connectivity and changes in bond damage and stress, Fig. 18 presents, for each probe bin, (i) the relationship between changes in contact connectivity and damage, and (ii) the relationship between changes in connectivity and changes in stress around the pile (see the figure below) using a Spearman correlation. The Spearman correlation coefficient ranges

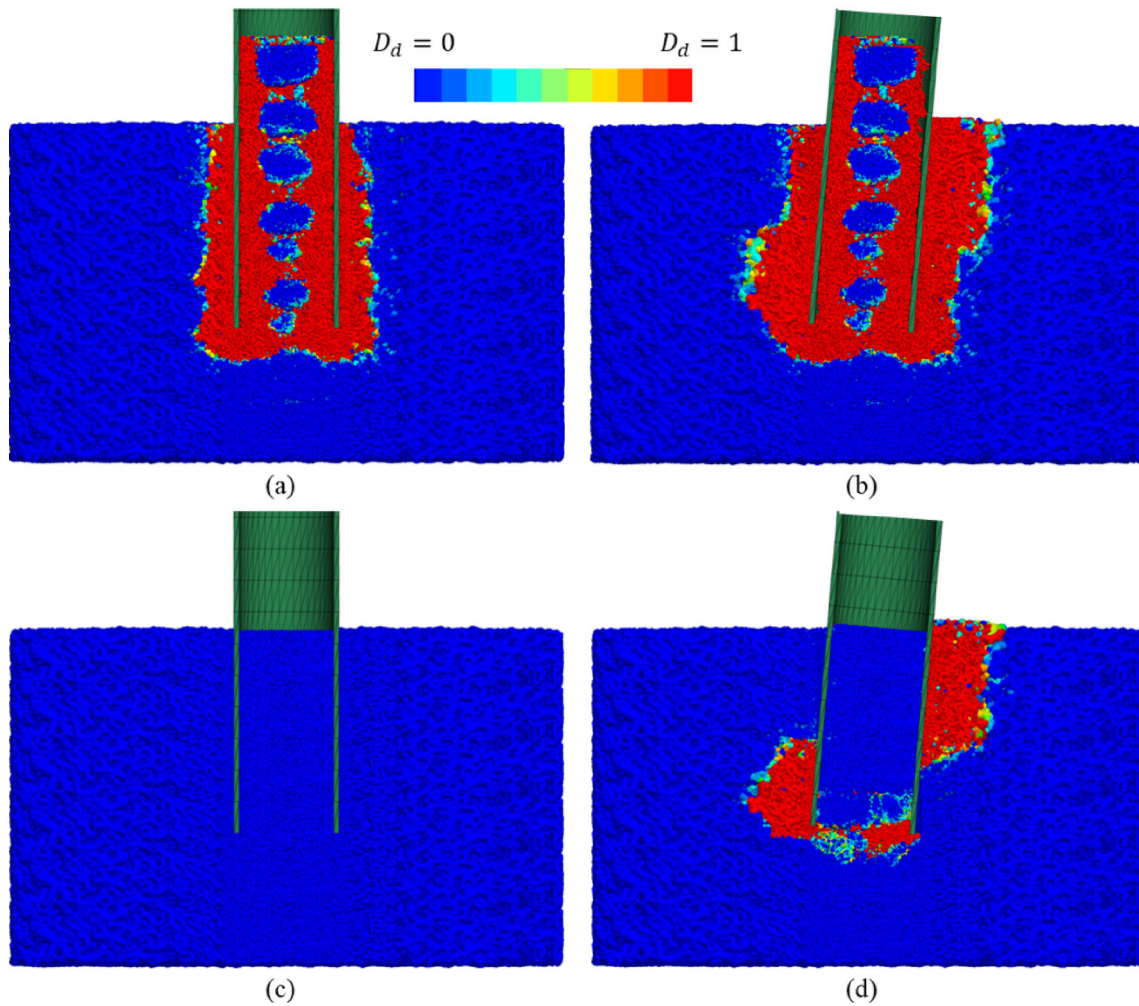


Fig. 16 Distribution of damage zone of the Pile B: **a** after installation; **b** after lateral loading of the jacked case; **c** after installation; **d** after lateral loading of the WIP case

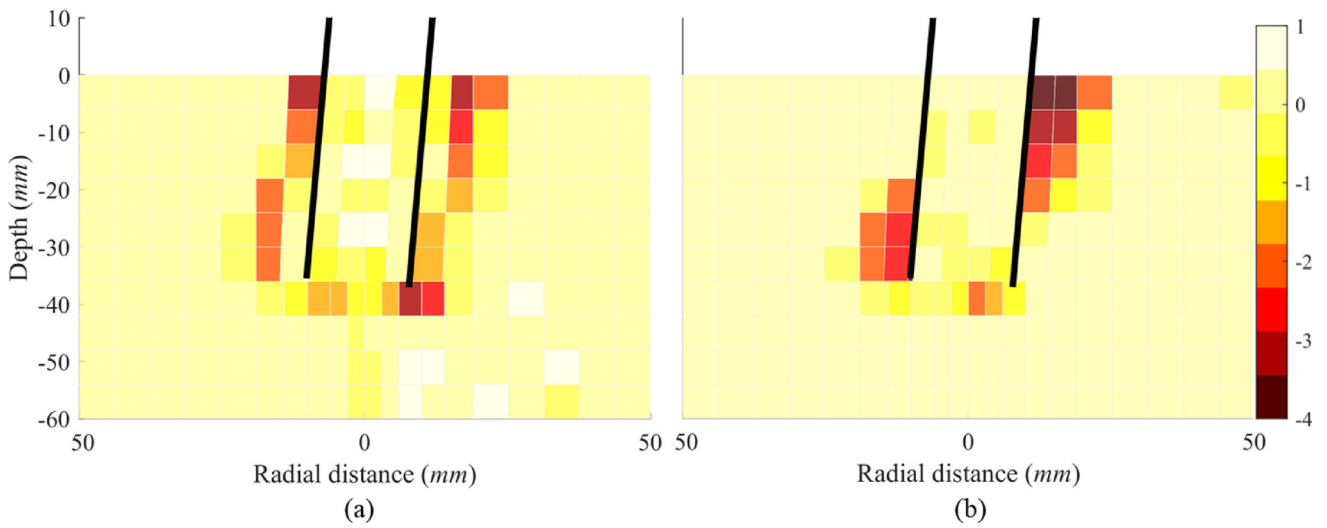


Fig. 17 Distribution of the change in contact connectivity of **a** jacked and **b** WIP Pile B

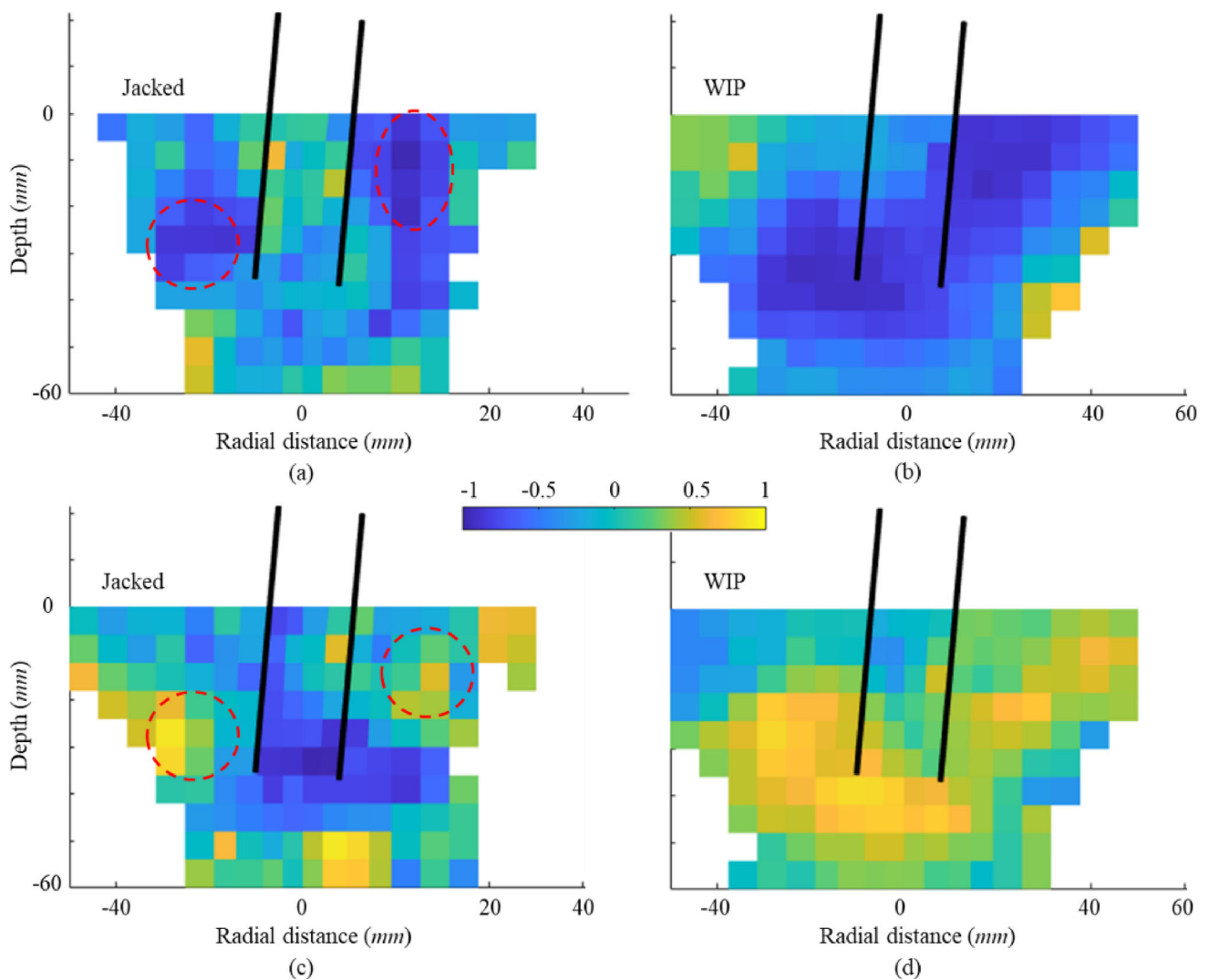


Fig. 18 Spearman correlation coefficient distribution: **a** and **b** the change in connectivity and damage of the jacked and WIP cases; **c** and **d** the change in connectivity and stress of the jacked and WIP cases

from -1 to 1 . A value greater than 0 indicates a positive monotonic relationship, while a value less than 0 signifies a negative one. The stress change was calculated as the difference between the stress before lateral loading and the stress after lateral loading (initial stress minus final stress).

The cell-based analysis results are shown in Fig. 18, with white areas indicating not a number (NaN). In the WIP pile case, particle connectivity demonstrates significant correlations with both damage and stress variations (Fig. 18b, d): an increase in damage shows a strong negative correlation with a decrease in connectivity, while a reduction in stress (negative in all grids for this case) exhibits a strong positive correlation with connectivity loss. For the jacked pile case, the passive zone in Fig. 18a reveals a strong negative correlation between damage change and connectivity change (marked by red circle), whereas no clear correlation is observed near the pile wall,

consistent with the stabilised connectivity around the pile shown in Fig. 17a. Meanwhile, the strong positive correlation between stress and connectivity (red circle in Fig. 18c) also corresponds to the stress increase zone in Fig. 15b. Moreover, the notable negative correlation below the pile tip in Fig. 18c indicates that lateral loading caused stress relief in this zone (defined as a positive stress change), transitioning the particle structure from dense to loose and thereby reducing connectivity.

6 Conclusions

A 3D coupled DEM-FDM model for open-ended piles installed in soft rocks has been built based on a recently developed scalable bond damage model. The installation effects for two different model piles section geometries

have been investigated, including the distribution of the stress field, porosity changes, the axial load transfer mechanism and effects on subsequent monotonic lateral loading. The numerical results are validated against two 1 g small-scale model tests, yielding the main conclusions as follows:

1. Limitations of traditional plugging indices: Due to the pronounced dilative behaviour of crushed particles in soft rocks, traditional plugging indices such as PLR and IFR fail to accurately describe the actual plugging state of OE piles. This study demonstrates that the interaction between internal arching structures and the nose cone ahead of the advancing pile base provides a more physically representative description of the plugging mechanism.
2. Microscale-based axial load-transfer mechanism: A microscale-based axial load-transfer mechanism for OE piles in soft rocks is proposed. The nose cone beneath the pile tip contributes to end bearing capacity (for plugged piles only), while external shearing provides external shaft resistance (for both plugged and unplugged piles) with negligible contribution from internal shaft friction. The magnitudes of both components are influenced by crack formation during installation. As most OWT piles have large values of D/t_w and therefore will not reach a fully plugged (or even partly plugged state), this study also microscopically validates the rationale behind the current ICP-18 design method for chalk, which assumes negligible internal shaft resistance.
3. Impact of installation effects on lateral stiffness: Although installation effects have limited influence on the ultimate lateral capacity, they significantly reduce the initial lateral stiffness by inducing microstructural damage and stress redistribution. This has important implications for predicting rock deformation around the pile under cyclic lateral loading and for assessing dynamic characteristics of OWT structures.
4. Micro–Macro-response linkage: By correlating changes in contact connectivity and bond damage distribution with local stress redistribution, failure zone expansion, and lateral stiffness reduction, this study establishes a clear link between microscale damage processes and the pile's macroscopic mechanical behaviour. The contrasting evolution of contact connectivity in corresponding zones around jacked and WIP piles demonstrates that installation-induced fine-grained annulus formation constitutes the primary factor governing their distinct initial lateral responses.

Particle upscaling improved computational efficiency, but it also reduced the pile wall-to-particle size ratio and

may introduce non-physical artefacts such as overly extensive bond-damage zones and unrealistically high porosity near the pile wall. Therefore, particle upscaling has inherent limits, and an appropriate balance between efficiency and accuracy must be carefully maintained in applying the approach presented herein to boundary value problems.

Acknowledgements This work is an output from the ICE-PICK project, funded by the New Investigator Award EPSRC grant EP/W00013X/1 and the RockMOOR project, funded by the Supergen Offshore Renewable Energy (ORE) Hub through the Flexible Funding grant (FFF2024-1076). The CSC scholarship (202008330363) supporting the first author is also acknowledged. Dr. Marco Previtali and Dr. Thomas Riccio are gratefully acknowledged for the fruitful discussions during the research progress.

Data availability The data that support the findings of this study are available from the corresponding author upon reasonable request.

Declarations

Conflict of interest The authors declare that they have no known conflict of interest or personal relationships that could have appeared to influence the work reported in this paper.

Open Access This article is licensed under a Creative Commons Attribution 4.0 International License, which permits use, sharing, adaptation, distribution and reproduction in any medium or format, as long as you give appropriate credit to the original author(s) and the source, provide a link to the Creative Commons licence, and indicate if changes were made. The images or other third party material in this article are included in the article's Creative Commons licence, unless indicated otherwise in a credit line to the material. If material is not included in the article's Creative Commons licence and your intended use is not permitted by statutory regulation or exceeds the permitted use, you will need to obtain permission directly from the copyright holder. To view a copy of this licence, visit <http://creativecommons.org/licenses/by/4.0/>.

References

1. Abhinav KA, Saha N (2015) Dynamic analysis of an offshore wind turbine including soil effects. *Procedia Eng* 116(1):32–39. <https://doi.org/10.1016/J.PROENG.2015.08.261>
2. Ahmadi-Naghadeh R, Liu T, Vinck K, Jardine RJ, Kontoe S, Byrne BW, McAdam RA (2022) A laboratory characterisation of the response of intact chalk to cyclic loading. *Géotechnique* 74(6):527–539
3. Alvarez-Borges F, Ahmed S, Madhusudhan BN, Richards D (2022) Investigation of pile penetration in calcareous soft rock using X-ray computed tomography. *Int J Phys Model Geotech* 22(1):38–52
4. Arroyo M, Butlanska J, Gens A, Calvetti F, Jamiolkowski M (2011) Cone penetration tests in a virtual calibration chamber. *Géotechnique* 61(6):525–531. <https://doi.org/10.1680/geot.9.P.067>
5. Barari A, Bagheri M, Rouainia M, Ibsen LB (2017) Deformation mechanisms for offshore monopile foundations accounting for cyclic mobility effects. *Soil Dyn Earthq Eng* 97:439–453. <https://doi.org/10.1016/j.soildyn.2017.03.008>

6. Been K, Jefferies MG (1985) A state parameter for sands. *Géotechnique* 35(2):99–112. <https://doi.org/10.1680/geot.1985.35.2.99>
7. Buckley RM, Jardine RJ, Kontoe S, Lehane BM (2018) Effective stress regime around a Jacked steel pile during installation ageing and load testing in chalk. *Can Geotech J* 55(11):1577–1591. <https://doi.org/10.1139/cgj-2017-0145>
8. Buckley RM, Jardine RJ, Kontoe S, Parker D, Schroeder FC (2018) Ageing and cyclic behaviour of axially loaded piles driven in chalk. *Géotechnique* 68(2):146–161. <https://doi.org/10.1680/jgeot.17.P.012>
9. Buckley RM, McAdam RA, Byrne BW et al (2020) Optimization of impact pile driving using optical fiber Bragg-grating measurements. *J Geotech Geoenviron Eng* 146(9):04020082. [https://doi.org/10.1061/\(ASCE\)GT.1943-5606.0002293](https://doi.org/10.1061/(ASCE)GT.1943-5606.0002293)
10. Cerfontaine B, Ciantia MO, Brown MJ, White DJ, Sharif YU (2023) DEM study of particle scale effect on plain and rotary jacked pile behaviour in granular materials. *Comput Geotech* 161:105559
11. Ciantia MO (2021) Installation effects on axial performance of monopiles in chalk for offshore renewables. In: Huynh DVK, Tang AH, Doan DH, Waston P (Eds.) *Proceedings of the 2nd Vietnam symposium on advances in offshore engineering*, Springer, Ho Chi Minh City, Vietnam, pp. 424–432, October 24 https://doi.org/10.1007/978-981-16-7735-9_47
12. Ciantia MO, Boschi K, Shire T, Emam S (2018) Numerical techniques for fast generation of large discrete-element models. *Proc Inst Civ Eng Comput Mech* 171(4):147–161. <https://doi.org/10.1680/jenclm.18.00025>
13. Ciantia MO, Castellanza R, Crosta GB, Hueckel T (2015) Effects of mineral softening and dissolution on strength and compressibility of soft carbonate rocks. *Eng Geol* 184:1–18
14. Ciantia MO, O'Sullivan, C, Jardine RJ (2019) Pile penetration in crushable soils: Insights from micromechanical modelling. In: da Fonseca AV, Mayne PW (Eds.) *Proceedings of the 17th European conference on soil mechanics and geotechnical engineering*, Reykjavik, Iceland, pp 298–317, September 1–6 <https://doi.org/10.32075/17ECSMGE-2019-1111>
15. Ciavaglia F, Carey J, Diambra A (2017) Monotonic and cyclic lateral tests on driven piles in chalk. *Geotech Eng* 170(4):353–366
16. Corciulo S, Zanolì O, Pisanò F (2017) Transient response of offshore wind turbines on monopiles in sand: role of cyclic hydro-mechanical soil behaviour. *Comput Geotech* 83:221–238. <https://doi.org/10.1016/j.compgeo.2016.11.010>
17. Cuéllar P, Mira P, Pastor M, Fernández Merodo JA, Baeßler M, Rücker W (2014) A numerical model for the transient analysis of offshore foundations under cyclic loading. *Comput Geotech* 59:75–86. <https://doi.org/10.1016/J.COMP GEO.2014.02.005>
18. De Nicola A, Randolph MF (1997) The plugging behaviour of driven and jacked piles in sand. *Géotechnique* 47(4):841–856. <https://doi.org/10.1680/geot.1997.47.4.841>
19. Doherty P, Gavin K (2011) Shaft capacity of open-ended piles in clay. *J Geotech Geoenviron Eng* 137(11):1090–1102. [https://doi.org/10.1061/\(ASCE\)GT.1943-5606.0000528](https://doi.org/10.1061/(ASCE)GT.1943-5606.0000528)
20. Falagush O, McDowell GR, Yu HS (2015) Discrete element modeling of cone penetration tests incorporating particle shape and crushing. *Int J Geomech* 15(6):04015003
21. Fan S, Bienen B, Randolph MF (2021) Centrifuge study on effect of installation method on lateral response of monopiles in sand. *Int J Phys Model Geotech* 21(1):40–52
22. Gavin K, Kovacevic MS, Igoe D (2021) A review of CPT based axial pile design in the Netherlands. *Undergr Space* 6(1):85–99. <https://doi.org/10.1016/J.UNDSP.2019.09.004>
23. Hong Y, He B, Wang LZ, Wang Z, Ng CWW, Mašin DJCGJ (2017) Cyclic lateral response and failure mechanisms of semi-rigid pile in soft clay: centrifuge tests and numerical modelling. *Can Geotech J* 54(6):806–824
24. Hu Q, Han F, Prezzi M, Salgado R, Zhao M (2022) Lateral load response of large-diameter monopiles in sand. *Géotechnique* 72(12):1035–1050
25. Huang X, Hanley KJ, O'Sullivan C, Kwok FC (2014) Effect of sample size on the response of DEM samples with a realistic grading. *Particuology* 15:107–115. <https://doi.org/10.1016/j.partic.2013.07.006>
26. Itasca Consulting Group, Inc. (2018) PFC3D 3-dimensional particle flow code
27. Janda A, Ooi JY (2016) DEM modeling of cone penetration and unconfined compression in cohesive solids. *Powder Technol* 293:60–68. <https://doi.org/10.1016/J.POWTEC.2015.05.034>
28. Jardine R, Chow F, Overy R, Standing J (2005) ICP design methods for driven piles in sands and clays. Thomas Telford Ltd, London
29. Jardine RJ, Buckley RM, Kontoe S, Barbosa P, Schroeder FC (2018) Behaviour of piles driven in chalk. In: *Engineering in chalk: proceedings of the chalk 2018 conference*, ICE publishing, pp 33–51
30. Jardine RJ, Buckley RM, Liu T et al (2024) The axial behaviour of piles driven in chalk. *Géotechnique* 74(6):553–569. <https://doi.org/10.1680/jgeot.22.00135>
31. Jenck O, Obaei A, Emeriault F, Dano C (2021) Effect of horizontal multidirectional cyclic loading on piles in sand: a numerical analysis. *J Mar Sci Eng* 9(2):235. <https://doi.org/10.3390/jmse9020235>
32. Jeong S, Ko J, Won J, Lee K (2015) Bearing capacity analysis of open-ended piles considering the degree of soil plugging. *Soils Found* 55(5):1001–1014. <https://doi.org/10.1016/J.SANDF.2015.06.007>
33. Ko J, Jeong S (2015) Plugging effect of open-ended piles in sandy soil. *Can Geotech J* 52(5):535–547. <https://doi.org/10.1139/cgj-2014-0041>
34. Lee J, Salgado R, Paik K (2003) Estimation of load capacity of pipe piles in sand based on cone penetration test results. *J Geotech Geoenviron Eng* 129(5):391–403. [https://doi.org/10.1061/\(ASCE\)1090-0241\(2003\)129:6\(391\)](https://doi.org/10.1061/(ASCE)1090-0241(2003)129:6(391))
35. Li L, Wu W, Hesham El Naggar M, Mei G, Liang R (2019) DEM analysis of the sand plug behavior during the installation process of open-ended pile. *Comput Geotech* 109:23–33. <https://doi.org/10.1016/J.COMP GEO.2019.01.014>
36. Li L, Wu W, Liu H, Lehane B (2021) DEM analysis of the plugging effect of open-ended pile during the installation process. *Ocean Eng* 220:108375. <https://doi.org/10.1016/J.OCEANENG.2020.108375>
37. Liu J, Duan N, Cui L, Zhu N (2019) DEM investigation of installation responses of jacked open-ended piles. *Acta Geotech* 14(6):1805–1819. <https://doi.org/10.1007/s11440-019-00817-7>
38. Liu T, Ahmadi-Naghadeh R, Vinck K, Jardine RJ, Kontoe S, Buckley RM, Byrne BW (2022) An experimental investigation into the behaviour of destructured chalk under cyclic loading. *Géotechnique* 74(6):540–552
39. Liu T, Ferreira PMV, Vinck K, Coop MR, Jardine RJ, Kontoe S (2023) The behaviour of a low- to medium-density chalk under a wide range of pressure conditions. *Soils Found* 63(1):101268. <https://doi.org/10.1016/J.SANDF.2022.101268>
40. Lord JA, Clayton CRI, Mortimore RN (2002) *Engineering in chalk*, Ciria C574. Construction Industry Research and Information Association, London
41. Lüking J, Kempfert HG (2013) Plugging effect of open-ended displacement piles. In: Delage P, Desrues J, Frank R, Puech A, Schlosser F (Eds) *Proceedings of the 18th international conference on soil mechanics and geotechnical engineering*, Paris, France, pp 2363–2366, September 2–6

42. Martinelli M, Pisanò F (2022) Relating cone penetration resistance to sand state using the material point method. *Geotech Lett* 12(2):131–138. <https://doi.org/10.1680/jgele.21.00145>
43. McAdam RA, Buckley RM, Schranz F, Byrne BW, Jardine RJ, Kontoe S, Crispin JJ (2025) Monotonic and cyclic lateral loading of piles in low-to medium-density chalk. *Géotechnique*. 75(13):164–180. <https://doi.org/10.1680/jgeot.23.00484>
44. McDowell GR, Falagush O, Yu HS (2012) A particle refinement method for simulating DEM of cone penetration testing in granular materials. *Geotech Lett* 2(3):141–147. <https://doi.org/10.1680/geolett.12.00036>
45. Monforte L, Arroyo M, Carbonell JM, Gens A (2022) Large-strain analysis of undrained smooth tube sampling. *Geotech* 72(1):61–77
46. Muirwood A, Mackenzie B, Burbury D, Rattley M, Clayton CRI, Mygind M, Andersen KW, Thilsted CL, Liingaard MA (2015) Design of large diameter monopiles in chalk at westernmost rough offshore wind farm. In: *Proceedings of the 3rd International Symposium on Frontiers in Offshore Geotechnics*, Perth, Australia, pp 723–728 <https://doi.org/10.1201/b18442-99>
47. Murff JD, Hamilton JM (1993) P-ultimate for undrained analysis of laterally loaded piles. *J Geotech Geoenviron Eng* 119(1):91–107
48. Murthy DS, Robinson RG, Rajagopal K (2021) Formation of soil plug in open-ended pipe piles in sandy soils. *Int J Geotech Eng* 15(5):519–529
49. Paik KH, Lee SR (1993) Behavior of soil plugs in open-ended model piles driven into sands. *Mar Georesour Geotechnol* 11(4):353–373
50. Paik K, Salgado R (2003) Determination of bearing capacity of open-ended piles in sand. *J Geotech Geoenviron Eng* 129(1):46–57
51. Paikowsky SG, Whitman RV (1990) The effects of plugging on pile performance and design. *Can Geotech J* 27(4):429–440. <https://doi.org/10.1139/t90-059>
52. Paikowsky SG, Whitman RV, Baligh MM (1989) A new look at the phenomenon of offshore pile plugging. *Mar Geotechnol* 8(3):213–230. <https://doi.org/10.1080/1064198909379869>
53. Pedone G, Kontoe S, Zdravković L et al (2023) Numerical modelling of laterally loaded piles driven in low-to-medium density fractured chalk. *Comput Geotech* 156:105252. <https://doi.org/10.1016/j.compgeo.2023.105252>
54. Previtali M, Ciantia MO, Riccio T (2023) Numerical installation of OE piles in soft rocks within the GPFEM framework. In: Zdravkovic L, Kontoe S, Tsaimpousi K, Taborda D (Eds) *Proceedings of the 10th European conference on numerical methods in geotechnical engineering*, CRC Press, London, June 26–28
55. Randolph MF, May M, Leong EC, Hyden AM, Murff JD (1992) Soil plug response in open-ended pipe piles. *J Geotech Eng* 118(5):743–759. [https://doi.org/10.1061/\(ASCE\)0733-9410\(1992\)118:5\(743\)](https://doi.org/10.1061/(ASCE)0733-9410(1992)118:5(743))
56. Riccio T (2025) Experimental observations on the behaviour of axially and laterally loaded piles installed in soft rock (Doctoral dissertation, University of Dundee)
57. Riccio T, Ciantia M (2024) Cooling prize paper: pile installation effects and plugging in soft rock. *Ground Eng*
58. Spyridis M, Lopez-Querol S (2024) Installation of open-ended piles: a numerical investigation into the effects on the state of silica sand. *Soils Found* 64(3):101458. <https://doi.org/10.1016/j.sandf.2024.101458>
59. Staubach P, Macháček J, Wichtmann T (2021) Large-deformation analysis of pile installation with subsequent lateral loading: Sanisand vs. hypoplasticity. *Soil Dyn Earthq Eng* 151:106964
60. Staubach P, Macháček J, Bienen B, Wichtmann T (2022) Long-term response of piles to cyclic lateral loading following vibratory and impact driving in water-saturated sand. *J Geotech Geoenviron Eng* 148(11):04022097
61. Taborda DMG, Zdravkovic L, Potts DM, Burd HJ, Byrne BW, Gavin KG, Houlsby GT, Jardine RJ, Liu T, Martin CM, McAdam RA (2020) Finite-element modelling of laterally loaded piles in a dense marine sand at Dunkirk. *Géotechnique* 70(11):1014–1029. <https://doi.org/10.1680/jgeot.18.PISA.006>
62. Vinck K, Liu T, Jardine RJ, Kontoe S, Ahmadi-Naghadeh R, Buckley RM (2024) Advanced in situ and laboratory characterisation of the ALPACA chalk research site. *Géotechnique* 74(6):512–526
63. Wang L, Zhou W, Guo Z, Rui S (2020) Frequency change and accumulated inclination of offshore wind turbine jacket structure with piles in sand under cyclic loadings. *Ocean Eng* 217:108045. <https://doi.org/10.1016/J.OCEANENG.2020.108045>
64. Wang T, Zhang Y, Bao X, Wu X (2020) Mechanisms of soil plug formation of open-ended jacked pipe pile in clay. *Comput Geotech* 118:103334. <https://doi.org/10.1016/J.COMPGeo.2019.103334>
65. Wellmann C, Wriggers P (2012) A two-scale model of granular materials. *Comput Methods Appl Mech Eng* 205:46–58. <https://doi.org/10.1016/J.CMA.2010.12.023>
66. Wen K, Kontoe S, Jardine R, Liu T (2024) Finite element modelling of pipe piles driven in low-to-medium density chalk under monotonic axial loading. *Comput Geotech* 172:106458. <https://doi.org/10.1016/J.COMPGeo.2024.106458>
67. White DJ, Bolton MD (2004) Displacement and strain paths during plane-strain model pile installation in sand. *Géotechnique* 54(6):375–397. <https://doi.org/10.1680/geot.2004.54.6.375>
68. Xu Z, Zhang L, Zhou S (2021) Influence of encasement length and geosynthetic stiffness on the performance of stone column: 3D DEM-FDM coupled numerical investigation. *Comput Geotech* 132:103993. <https://doi.org/10.1016/j.compgeo.2020.103993>
69. Yang ZX, Gao YY, Jardine RJ, Guo WB, Wang D (2020) Large deformation finite-element simulation of displacement-pile installation experiments in sand. *J Geotech Geoenviron Eng* 146(6):04020044. [https://doi.org/10.1061/\(asce\)gt.1943-5606.0002271](https://doi.org/10.1061/(asce)gt.1943-5606.0002271)
70. Zhang X, Fatahi B (2021) Assessing axial load transfer mechanism of open-ended tubular piles penetrating in weak rocks using three-dimensional discrete element method. *Comput Geotech* 137:104267. <https://doi.org/10.1016/j.compgeo.2021.104267>
71. Zheng JH, Qi CG, Zhao X, Wang XQ, Shan YL (2020) Experimental simulation on open-ended pipe pile penetration using transparent granule. *KSCE J Civ Eng* 24(8):2281–2292. <https://doi.org/10.1007/s12205-020-1235-3>
72. Zheng J, Previtali M, Knappett JA, Ciantia MO (2022) Coupled DEM-FDM investigation of centrifuge acceleration on the response of shallow foundations in soft rocks. In: Chung M, Kim K, Kim N, Kwon T, Park, H, Jo S, Kim J (Eds) *Physical modelling in geotechnics: Proceedings of the 10th international conference on physical modelling in geotechnics*, Daejeon, South Korea, pp 264–267, September 19–23
73. Zheng J, Ciantia MO (2025) An efficient damage-plasticity DEM contact model for highly porous rocks. *Rock Mech Rock Eng* 58(5):5733–5754
74. Zhou W, Guo Z, Wang L, Li J, Li Y, Rui S (2021) Simplified t-z models for estimating the frequency and inclination of jacket supported offshore wind turbines. *Comput Geotech* 132:103959. <https://doi.org/10.1016/J.COMPGeo.2020.103959>
75. Zhuang PZ, Yue HY, Song XG, Yang H, Yu HS (2021) uplift behavior of pipes and strip plate anchors in sand. *J Geotec Geoenviron Eng* 147(11):04021126. [https://doi.org/10.1061/\(ASCE\)GT.1943-5606.000267](https://doi.org/10.1061/(ASCE)GT.1943-5606.000267)